JGR Atmospheres

RESEARCH ARTICLE
10.1029/2020JD034090

Changes in Clear-Sky Shortwave Aerosol Direct Radiative Effects Since 2002

Norman G. Loeb[1], Wenying Su[1], Nicolas Bellouin[2], and Yi Ming[3]

[1]NASA Langley Research Center, Hampton, VA, USA, [2]Department of Meteorology, University of Reading, Reading, UK, [3]NOAA/Geophysical Fluid Dynamics Laboratory, Princeton, NJ, USA

Key Points:

- Satellite observations show that radiative cooling by aerosols has significantly declined over North America since 2002
- During the COVID-19 shutdown, hot and humid conditions over northeastern China masked the influence of reduced aerosol emissions
- After accounting for meteorology, aerosol radiative cooling over northeastern China is reduced by up to 23% in early 2020

Supporting Information:

- Supporting Information S1

Correspondence to:
N. G. Loeb,
norman.g.loeb@nasa.gov

Citation:
Loeb, N. G., Su, W., Bellouin, N., & Ming, Y. (2021). Changes in clear-sky shortwave aerosol direct radiative effects since 2002. *Journal of Geophysical Research: Atmospheres*, *126*, e2020JD034090. https://doi.org/10.1029/2020JD034090

Received 15 OCT 2020
Accepted 4 FEB 2021

Abstract A new method for determining clear-sky shortwave aerosol direct radiative effects (ADRE) from the Clouds and the Earth's Radiant Energy System is used to examine changes in ADRE since 2002 alongside changes in aerosol optical depth (AOD) from the Moderate Resolution Spectroradiometer. At global scales, neither ADRE nor AOD show a significant trend. Over the northern hemisphere (NH), ADRE increases by 0.18 ± 0.17 Wm^{-2} per decade (less reflection to space) but shows no significant change over the southern hemisphere. The increase in the NH is primarily due to emission reductions in China, the United States, and Europe. The COVID-19 shutdown shows no noticeable impact on either global ADRE or AOD, but there is a substantial influence over northeastern China in March 2020. In contrast, February 2020 anomalies in ADRE and AOD are within natural variability even though the impact of the shutdown on industry was more pronounced in February than March. The reason is because February 2020 was exceptionally hot and humid over China, which compensated for reduced emissions. After accounting for meteorology and normalizing by incident solar flux, February ADRE anomalies increase substantially, exceeding the climatological mean ADRE by 23%. February and March 2020 correspond to the only period in which adjusted anomalies exceed the 95% confidence interval for 2 consecutive months. Distinct water-land differences over northeastern China are observed in ADRE but not in AOD. This is likely due to the influence of surface albedo on ADRE in the presence of absorbing aerosols.

1. Introduction

Climate is fueled by how much of the sun's energy is absorbed by Earth. Emission of aerosols into the atmosphere, whether natural or anthropogenic, has a direct impact on how much solar energy is reflected, absorbed, and transmitted by the atmosphere. Under cloud-free conditions, which occurs roughly one-third of the time globally, the dominant radiative effects of aerosols are the reflection of incident solar radiation back to space and direct absorption of sunlight in the atmosphere. These reduce how much solar energy is available at the surface, affecting atmospheric circulation and turbulent heat exchanges between the surface and atmosphere (Evan et al., 2011; Ramanathan et al., 2001). Under cloudy skies, aerosols influence cloud microphysical properties and albedo, further altering Earth's energy budget. The indirect effect of aerosols on Earth's radiation budget through cloud changes is highly uncertain due to the complexity of the aerosol-cloud-radiation interactions (Bellouin, Quaas, et al., 2020).

Satellite observations have significantly improved our understanding of the temporal and spatial distributions of aerosols, clouds, and radiation. Much has been learned about the mean optical and radiative properties of aerosols and clouds and how they influence and are influenced by the Earth's radiation budget (Ackerman et al., 2019; Ceppi & Hartmann, 2015; Loeb et al., 2016; Mace & Berry, 2017). With the emergence of long observational records from instruments with advanced onboard calibration systems in stable orbits, there is increasing interest in using satellite observations to study longer term changes in aerosols, clouds and radiation (Hammer et al., 2020; Hsu et al., 2019; Kato et al., 2020; Loeb, Thorsen, et al., 2018; Sawyer et al., 2020; Su et al., 2020; Yuan et al., 2018). Prior to the launch of instruments aboard the Terra and Aqua platforms (Imhoff et al., 2009; Parkinson et al., 2013), many of the imagers used for aerosol and cloud trends had no onboard calibration sources in the visible and required large adjustments to account for orbital drifts that cause the mean local time (MLT) of the measurements to change over the course of the mission (Bhatt et al., 2016; Brest & Rossow, 1992; Heidinger et al., 2010; Karlsson et al., 2013; Mishchenko et al., 2007). Since 2000, the Clouds and the Earth's Radiant Energy System (CERES) and the Moderate Resolution Spectroradiometer (MODIS) instruments aboard the Terra and Aqua satellites have been providing

the longest running global records of aerosols, clouds, and radiation budget from instruments that benefit from onboard and vicarious calibration and satellite orbits with fixed MLTs, making them the most suitable datasets available for studying variations since 2000.

In this study, we use observations from CERES and MODIS to examine changes in clear-sky aerosol direct radiative effect (ADRE) and aerosol optical depth (AOD) between July 2002 and March 2020 at global and regional scales. In addition to examining regional and global trends, we analyze anomalies over China during the unprecedented COVID-19 global shutdown and investigate the role that meteorology had on the anomalies. We use a novel analysis technique that separates atmospheric from surface contributions to SW TOA flux to separate the influence of atmospheric and surface variations on ADRE. Sections 2.1–2.3 describe the data and methodology used to determine ADRE from CERES data. Section 2.4 describes how meteorological variability is assessed over China. Section 3 describes the results and a brief summary is given in Section 4.

2. Data and Methods

2.1. ADRE Determination

The ADRE is the difference between the SW TOA flux (F) for a pristine atmosphere with no aerosol and the actual atmosphere with aerosol optical depth τ_a:

$$\text{ADRE} = F\left(0, \alpha; x_1, x_2, \ldots x_n\right) - F\left(\tau_a, \alpha; x_1, x_2, \ldots x_n\right) \tag{1}$$

where α is surface albedo and x_1, x_2, ..., x_n correspond to atmospheric variables other than τ_a and α that influence SW TOA flux (e.g., water vapor, trace gases, incoming solar irradiance). A deseasonalized monthly anomaly (δy) of a given variable y is obtained from the difference between the monthly mean of y and its corresponding monthly climatology $\left(\overline{y}\right)$, determined by averaging all years of the same month. The deseasonalized anomaly in ADRE is thus:

$$\delta\text{ADRE} = \delta F\left(0, \alpha\right) - \delta F\left(\tau_a, \alpha\right) \tag{2}$$

For brevity, in Equation 2 and henceforth, we drop the x_1, x_2, ..., x_n variables in the equations (however their influence on ADRE is accounted for in the data). In practice, TOA flux variations in the pristine-sky case ($\delta F\left(0, \alpha\right)$) cannot be observed directly since aerosols cannot be instantaneously removed from observations. As described below, here we use a combination of calculated fluxes in the CERES SYN1deg-Month Edition 4A (Rutan et al., 2015) data product and observed fluxes in the Energy Balanced and Filled (EBAF) Ed4.1 product (Loeb, Doelling, et al., 2018) to determine δADRE. The second term on the right-hand-side of Equation 2 can be expressed as follows:

$$\delta F\left(\tau_a, \alpha\right) = \delta F\left(\text{ATM}\right) + \delta F\left(\text{SFC}\right) \tag{3}$$

The first term on the right-hand-side corresponds to the TOA flux anomaly resulting from atmospheric variations (i.e., in τ_a,x_1, x_2, ..., x_n) for a surface albedo held fixed at its climatological value ($\overline{\alpha}$). The second term accounts for variations in α for a climatological atmosphere. To determine the atmospheric and surface contributions, we use the Decomposition Method described in Loeb et al. (2019). Substituting Equation 3 into Equation 2 yields:

$$\delta\text{ADRE} = -\delta F\left(\text{ATM}\right) + \left[\delta F\left(0, \alpha\right) - \delta F\left(\text{SFC}\right)\right] \tag{4}$$

The first term on the right-hand-side of Equation 4 is determined by applying the Decomposition Method to the observed EBAF Ed4.1 flux, retaining only the atmospheric contribution. The difference between the last two terms on the right-hand-side accounts for the masking effect of aerosols on surface albedo variations simply due to the presence of aerosols. We obtain $\delta F\left(0, \alpha\right)$ from the CERES SYN1deg Pristine-sky

TOA flux. For consistency, we also use CERES SYN1deg calculated fluxes to determine $\delta F\left(\mathrm{SFC}\right)$ from the Decomposition Method. With this approach, δADRE is directly related to the atmospheric contribution from EBAF observations, while SYN1deg calculations are only used in the aerosol masking term. Since the masking term is a difference determined using consistent input variables, input errors in the calculations (e.g., surface albedo) will have less impact on δADRE compared to direct use of Equation 2.

2.2. Decomposition of Clear-Sky SW TOA Flux Anomalies

Clear-sky SW ADRE anomalies are decomposed into atmospheric (ATM) and surface (SFC) contributions using the methodology described in Loeb et al. (2019). This method is an extension of a framework introduced by Stephens et al. (2015) in which the Earth–atmosphere system is represented as a reflecting and absorbing atmospheric layer above a reflecting surface. Stephens et al. (2015) provide a means of separating the atmosphere-only from atmosphere-surface SW contributions to TOA radiation using only radiative fluxes at the TOA and surface obtained from either observations or models. Loeb et al. (2019) extended the framework to provide a set of equations enabling calculation of ATM and SFC contributions to variations in reflected SW TOA and surface net downward radiative fluxes. The ATM contribution includes SW radiation variations associated with atmospheric variability with no interaction with the surface, and variations in which radiation interacts with a variable atmosphere and an invariant surface, with the latter specified from monthly climatological values of surface albedo. The SFC contribution is determined from the difference between the observed TOA flux anomaly and the corresponding anomaly associated with the ATM contribution.

2.3. Satellite Observations

Clear-sky TOA and surface radiative fluxes for 1° × 1° latitude-longitude regions are from the CERES EBAF Ed4.1 product (Kato et al., 2018; Loeb, Doelling, et al., 2018). We restrict our analysis to 07/2002–03/2020, which includes only Aqua data. We use all months between 07/2002 and 12/2019 to define the baseline climatology for calculating deseasonalized monthly anomalies over the analysis period. The first 3 months in 2020 are excluded from the baseline climatology in order to assess the influence of the COVID-19 period against prior years.

Clear-sky radiative fluxes are determined using radiance measurements for clear fields-of-view from both CERES and MODIS in order to provide complete global coverage monthly (Loeb, Doelling, et al., 2018). Surface radiative fluxes in EBAF Ed4.1 are constrained by the observed EBAF TOA fluxes by adjusting the initial inputs to the radiative transfer model calculations within their uncertainty ranges so that the TOA flux calculations match the observed values. Initial surface albedos and aerosol properties used in the calculations are described in Rutan et al. (2009, 2015). Kato et al. (2018) describe how surface fluxes in EBAF are constrained to the TOA observations. Initial AODs are from the Model of Atmospheric Transport and Chemistry (MATCH; Collins et al., 2001), which assimilates MODIS AODs to provide hourly AODs and aerosol type. MATCH uses climatological sources of aerosols except for wind driven dust and sea salt. Since climatological sources of aerosols are used in nondust conditions, any trends in aerosol absorption would not be accounted for in MATCH. This could lead to significant overestimations/underestimations in ADRE trends in regions with large changes in aerosol absorption (Tao et al., 2020).

To determine long-term changes in AOD, we use the MODIS MYD08_M3.061 550 nm AOD Dark Target + Deep Blue Combined product (Levy et al., 2013; Sayer et al., 2014), which also provides 1° × 1° latitude-longitude gridded data. We note that the cloud masks used to determine the MODIS AODs and CERES clear-sky TOA fluxes are different from one another. The cloud mask for MODIS AOD is based upon Frey et al. (2008), while for CERES clear-sky flux, it is based upon Trepte et al. (2019).

We consider only surfaces that are free of snow and ice as provided by the CERES SSF1deg Edition 4A product, which uses snow/ice maps from a combination of the National Snow and Ice Data Center (NSIDC) Near-Real Time Snow and Ice Extent (NISE) product (Brodzik & Stewart, 2016), the National Environmental Satellite, Data and Information Service (NESDIS) snow/ice map, and the CERES team's snow and sea ice fraction over the clear portions of CERES footprints (Trepte et al., 2019).

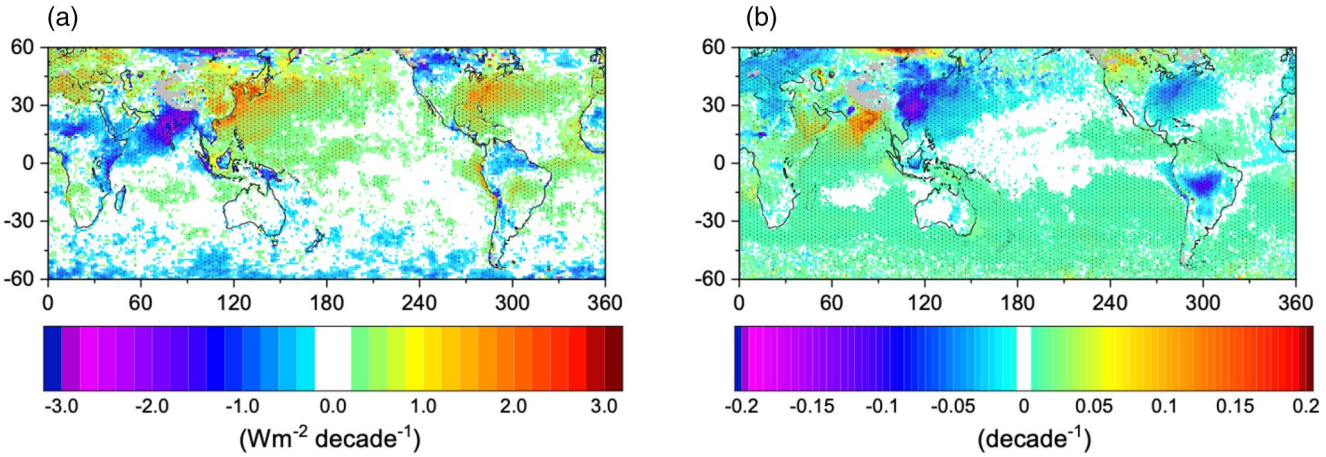

Figure 1. Trend in anomalies of (a) SW clear-sky ADRE and (b) AOD for 2002/07–2020/03. Stippled area exceeds 95% confidence interval. ADRE, aerosol direct radiative effects; AOD, aerosol optical depth.

2.4. Accounting for Regional Meteorological Variability

To account for variations in ADRE and AOD over China due to meteorology, we use a multilinear regression model that relates anomalies in ADRE and AOD with anomalies in the following variables: Niño 3.4 index, 2-m eastward wind (U2M), 2-m northward wind (V2M), Estimated Inversion Strength (EIS), 2-m air temperature (T2M), 2-m specific humidity (QV2M), and daytime average cloud fraction between the surface and 700 mb (f_L). The Niño 3.4 index is from the National Oceanic and Atmospheric Administration (NOAA) Earth System Research Laboratory (ESRL) and corresponds to a 5-month running mean of sea-surface temperature (SST) anomalies in the Niño 3.4 region (5°N–5°S, 120°–170°W). The Niño 3.4 index has recently been shown to influence aerosol concentrations over China (Feng et al., 2020). U2M, V2M, T2M, and QV2M are from the Modern-Era Retrospective Analysis for Research and Applications, Version 2 (MERRA-2) (Gelaro et al., 2017). The EIS provides an estimate of the strength of the planetary boundary layer (PBL) inversion given the temperatures at 700 hPa and at the surface (Wood & Bretherton, 2006). Here, EIS data from the CERES SSF1deg Edition 4A product are used. The f_L data provide an additional indication of atmospheric boundary layer moisture, as higher humidity in clear areas are expected when more low clouds are present in the same 1° × 1° gridbox. The f_L data are inferred from MODIS Aqua observations as provided in the CERES SSF1deg Edition 4A product.

We perform the multilinear regression analysis over China for 10°–50°N and 100°–180°E. While the data products considered are available at 1° × 1° latitude-longitude resolution, the regional multilinear regression analysis is only performed over a moving 9° × 9° latitude-longitude window in 1° increments in order to reduce sampling error in cloudy regions. Twelve sets of regression coefficients are determined, one for each calendar month. The regression coefficients are obtained using all occurrences of a given month and all occurrences of the preceding and following months (e.g., February regression coefficients are determined using data from all January, February, and March months over the record). Regression coefficients are determined using data from 07/2002 to 12/2019. Section S1, "Multilinear Regression," in the supporting information provides more background information about the multilinear regression analysis approach used in this study together with a specific example showing ADRE sensitivity to individual parameters along with anomalies and ADRE contributions of each parameter.

3. Results

3.1. Regional, Zonal, and Global ADRE and AOD Trends

Since 2002, marked changes in aerosol emissions have occurred over China, India, the United States, and Europe (Paulot et al., 2018; Zhao et al., 2017). Figures 1a and 1b show CERES ADRE and MODIS AOD trends for 07/2002–03/2020. Trends are determined using least squares linear regression. Uncertainties in the trends correspond to 5%–95% confidence intervals following the methodology in Santer et al. (2000).

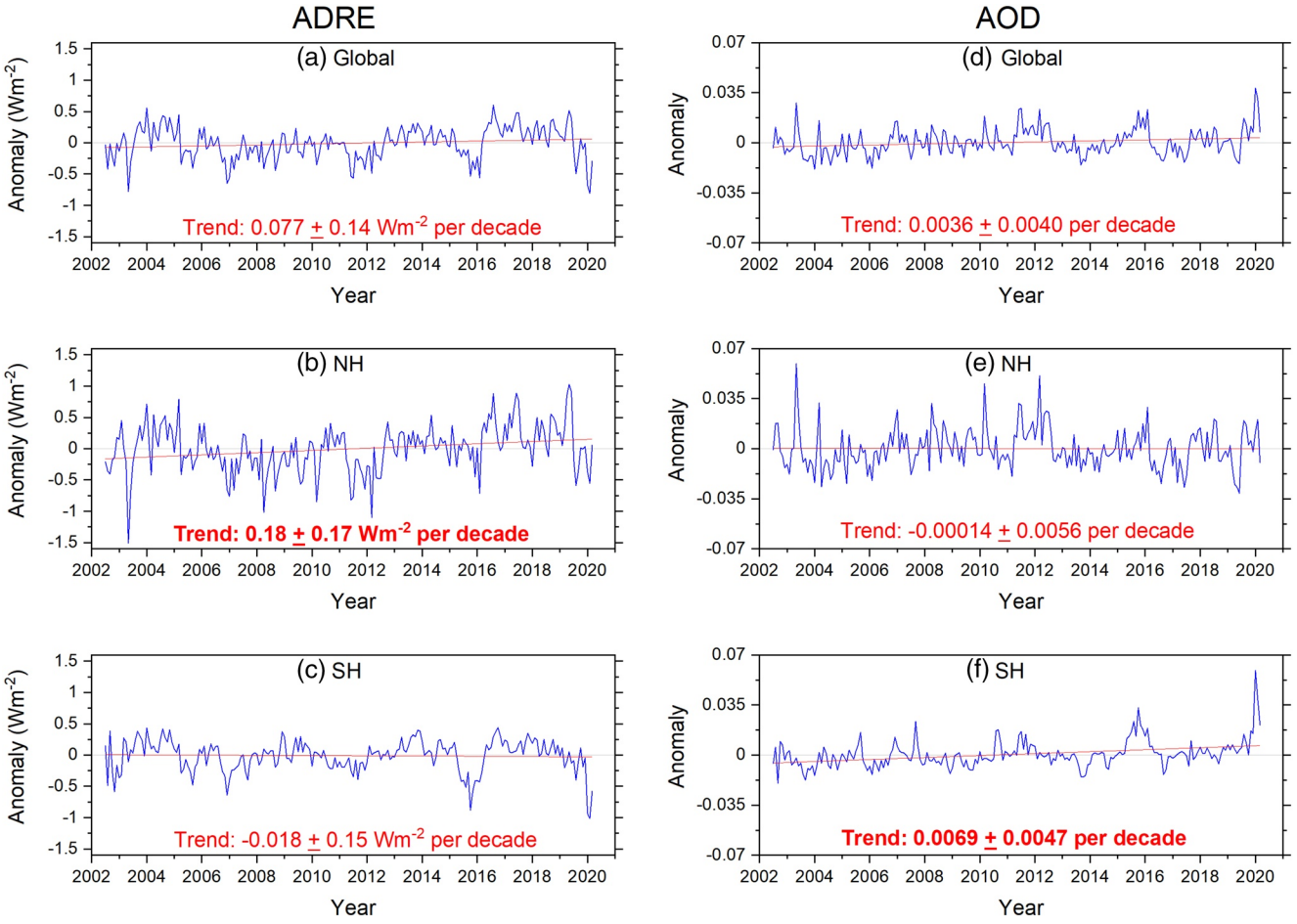

Figure 2. Anomalies in ADRE (left column) and AOD (right column) for (a and d) global, (b and e) NH, and (c and f) SH. Trend and 95% confidence intervals are shown in red. ADRE, aerosol direct radiative effects; AOD, aerosol optical depth; NH, northern hemisphere; SH, southern hemisphere.

Increases in ADRE (less reflection to space) and decreases in AOD occur over China, the United States, South America, and Europe. Conversely, ADRE decreases (more reflection to space) and AOD increases over India. These results are largely consistent with Paulot et al. (2018) (see their Figure 2), who also used CERES observations to determine ADRE with a different approach and time period (2001–2015). The most notable difference between results in Figure 1a and Paulot et al. (2018) occurs over mainland China. In Paulot et al. (2018), ADRE trends over land in eastern China are generally negative, while they are positive here. We suspect the difference is due to how surface albedo changes are accounted for in the two approaches as well as the different time periods used. Paulot et al. (2018) use model-based radiative kernels derived for aerosol-free conditions to "remove" variations in surface albedo, water vapor, and ozone from the observations. Because the radiative kernels are determined for aerosol-free conditions and applied to observations, the radiative kernels may not correctly account for surface albedo variations since aerosols were not included in their derivation.

Globally, ADRE increases by 0.08 ± 0.14 Wm^{-2} per decade (trend uncertainty given by 5%–95% confidence range) (Figure 2a). This is mainly due to a significant increase of 0.18 ± 0.17 Wm^{-2} per decade over the northern hemisphere (NH) (Figure 2b). Over the southern hemisphere (SH), the ADRE trend is near zero (−0.018 ± 0.15 Wm^{-2} per decade) (Figure 2c). Consistent with Remer et al. (2020), we do not see a trend in global mean AOD using the latest version of MODIS (Collection 6.1) (Figure 2d). However, the AOD trend is near-zero over the NH (Figure 2e) and reaches 0.0069 per decade over the SH, which exceeds the 95% confidence interval (Figure 2f).

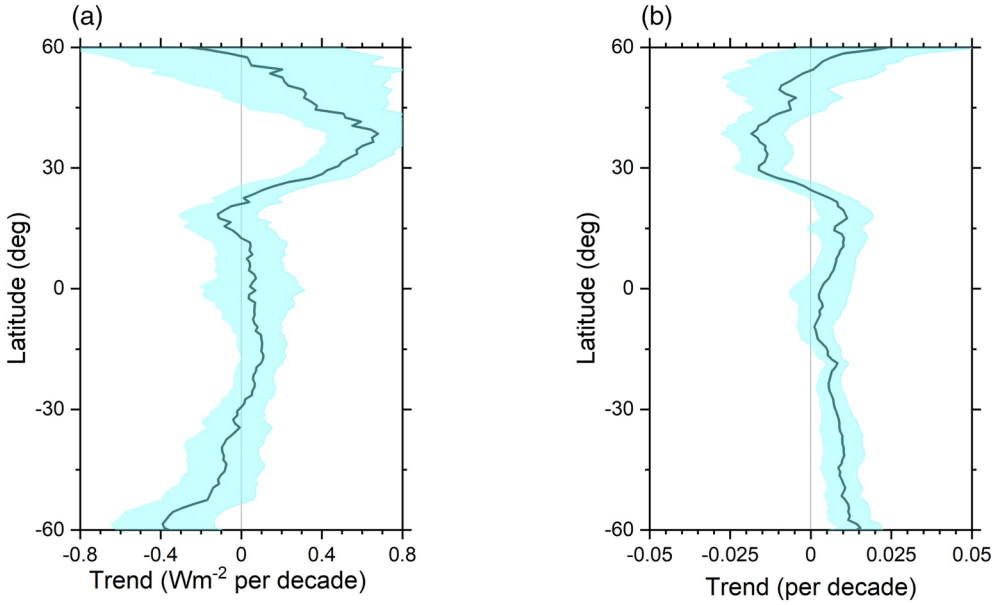

Figure 3. Trend in zonal mean anomalies of (a) SW clear-sky ADRE and (b) AOD for 2002/07–2020/03. Shaded regions correspond to 95% confidence interval. ADRE, aerosol direct radiative effects; AOD, aerosol optical depth.

The regional and zonal average ADRE trends in Figures 1a and 3a suggest that the positive NH trend in ADRE is a consequence of positive trends over China and North America overwhelming negative trends over India. In contrast, negative trends in AOD poleward of 20°N appear to cancel positive trends equatorward of 20°N (Figures 1b and 3b). In the SH, positive zonal average AOD trends exceed the 95% confidence interval poleward of 15°S (Figure 3b). Furthermore, the AOD trends are widespread, uniform and mainly occur over the SH oceans (Figure 1b). Positive AOD trends over the southern oceans are also apparent in Remer et al. (2020; see their Figure 12). Since the CERES results do not show this unexpected behavior, we cannot exclude MODIS calibration drift as a possible cause, as recently suggested by Bellouin, Davies, et al. (2020), who found similar results. On the other hand, if the SH AOD trends are real and are due to anthropogenic aerosols transported to the Southern Ocean, this would have important implications to aerosol radiative forcing. However, the reality of that transport is an open question, as discussed in Bellouin, Quaas, et al. (2020).

In spite of the inconsistencies in long-term trends between CERES ADRE and MODIS AODs, monthly anomalies are strongly anticorrelated (Figures 4a–4c). For the NH, which has the greatest range of variability, the *R*-square value is 0.81 (correlation coefficient of −0.90). The ADRE efficiency, determined from

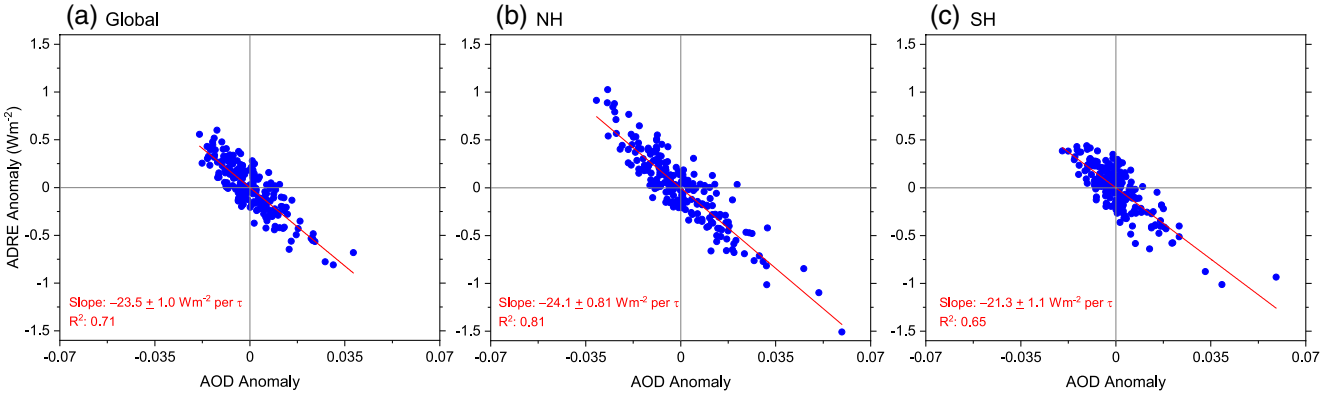

Figure 4. Scatterplots of ADRE against AOD monthly anomalies for (a) global, (b) NH, and (c) SH averages between 2002/07–2020/03. Red line corresponds to least squares fit. ADRE, aerosol direct radiative effects; AOD, aerosol optical depth; NH, northern hemisphere; SH, southern hemisphere.

the slope of the least squares fit in Figure 4, is approximately -24 ± 1.0 Wm^{-2} per τ globally. Appreciable ADRE and AOD NH anomalies appear in May 2003 (Figures 2b and 2c) due to biomass burning smoke from extensive forest fires in Siberia, Russia, which were transported across the Northern Pacific Ocean (Damoah et al., 2004; Lee et al., 2005). The large anomalies in the SH during September–October 2015 are due to smoke from massive fires over Indonesia (Koplitz et al., 2016). The pronounced negative ADRE anomalies (positive AOD anomalies) over the SH between November 2019 and March 2020 are due to the Australian bushfires (Figures 2c and 2f), which resulted in increased reflection from smoke that spread over much of the Southern Ocean region (Yu et al., 2020). We note that while the Australian bushfires contribute to the positive SH AOD trend, excluding the months between November 2019 and March 2020 still results in a significant positive AOD trend.

At hemispheric and global scales, there does not appear to be a noticeable influence of the COVID-19 shutdown during the first few months of 2020 (Figures 2a–2f). In fact, ADRE anomalies are negative and AOD anomalies are positive in each hemisphere, implying increased reflection. In contrast, the Australian bushfires appear to have a far more prominent global impact than COVID-19.

3.2. ADRE and AOD Over East Asia During COVID-19

Despite weak global effects, the COVID-19 shutdown did have a noticeable impact on ADRE and AOD over China and the East Asian Marginal Seas. In China, the shutdown started in late January 2020. By the end of February and continuing through March, China gradually reopened its factories and businesses. The shutdown had its greatest impact on manufacturing in February, with a sharp decline in the Purchasing Managers' Index, a measure of economic activity in the Chinese manufacturing sector (Diamond & Wood, 2020; Harris, 1991). Several studies have shown that reductions in primary emissions were largely compensated by secondary particulate pollution during warm and moist meteorological conditions, resulting in haze events in many cities (Chang et al., 2020; Diamond & Wood, 2020; Field et al., 2020; Huang et al., 2020; Le et al., 2020; Wang et al., 2020). Winter haze events in eastern China have been increasing in frequency in recent decades (Y. Yang et al., 2016). Diamond and Wood (2020) argue that sharp declines in nitrogen dioxide resulted from a marked decrease in transportation while particulate emissions were less impacted since they are primarily produced by industry and power generation, which were less affected by the shutdown compared to transportation. Here we find that when meteorological influences are accounted for, the COVID-19 shutdown had a marked impact on ADRE and AOD during February and March 2020.

Anomalies in ADRE and AOD for February and March 2020 are shown in Figures 5a–5d. During both months, ADRE increases and AOD decreases between 25°N–45°N and 110°E–140°E. The ADRE anomaly increases are much more pronounced in March than in February. By comparison, the contrast in AOD between February and March (Figures 5b and 5d) is far less pronounced.

To get a sense of the influence of meteorology on ADRE, we apply the multilinear regression model described in Section 2.4. The explained variance for February and March months as provided by the regression R-squared value is provided in Figures 6a and 6b. The multilinear regression explains up top 80% of the variability in ADRE over the northern portion of the Yellow Sea and adjacent land regions. With the exception of a small area around 10°N near the Date Line, the multilinear regression over the ocean areas to the east and south of the Yellow Sea region accounts for <40% of the variability. In contrast, R-squared values during summertime are smaller than in winter (not shown) presumably because there is less synoptic variability during summertime. As noted earlier, the multilinear regression model is applied to data over a moving 9° × 9° latitude-longitude window in 1° increments. We also ran the analysis using 3° × 3° and 5° × 5° moving windows (Figure S3). We found that the 9° × 9° latitude-longitude window resulted in the highest overall regional R-squared values and therefore used that resolution to relate ADRE and AOD with large-scale meteorological conditions.

Figure 7 compares the February and March 2020 ADRE anomalies (Figures 7a and 7d) with those obtained from the multilinear regression analysis (Figures 7b and 7e). Interestingly, meteorological variations result in a large negative ADRE anomaly over the Yellow Sea region during February (Figure 7b) and a positive anomaly over the same region in March (Figure 7e). When the meteorological contributions in Figures 7b and 7e are subtracted from the corresponding ADRE anomalies in Figures 7a and 7d, anomalies over the

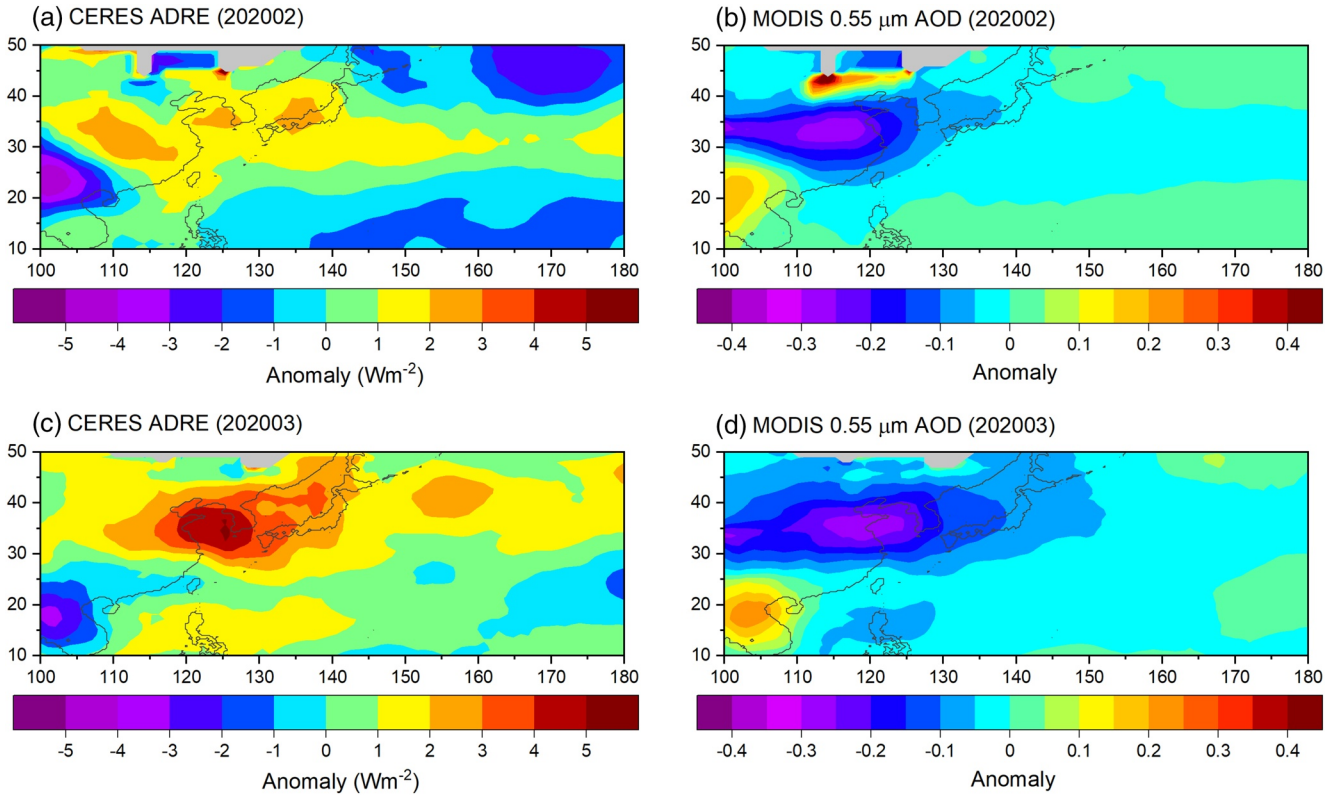

Figure 5. Anomalies of ADRE (a and c) and AOD (b and d) for February 2020 (top) and March 2020 (bottom). Gray areas correspond to areas contaminated by snow. ADRE, aerosol direct radiative effects; AOD, aerosol optical depth.

Yellow Sea region in February exceed those in March (Figures 7c and 7f). If we further account for differences in incoming solar radiation by dividing ADRE by solar flux in each month (Figures 8a–8f), the contrast between February and March is even more apparent (Figures 8c and 8f). A similar analysis is shown for AOD in Figures 9a–9f. After accounting for meteorology, negative anomalies over northeast China are more pronounced in February than in March, consistent with the ADRE results.

We note that the peak negative AOD anomaly in February (Figure 9c) occurs over land to the southwest of the maximum in normalized ADRE (Figure 8c). A possible reason for this difference is because ADRE depends not only on AOD, but also on surface albedo (Derimian et al., 2016). When surface albedo is low, the SW cooling effect of aerosol for a given AOD increase is greater than for a surface with a higher albedo. Since the surface albedo of water is much smaller than land, sensitivity to the AOD decrease throughout the region is greater over the Yellow Sea region. A second reason relates to the ADRE dependence on surface albedo variations through the aerosol masking term in Equation 4. It turns out that this contribution is primarily negative (reaching $-1.8\ \mathrm{Wm}^{-2}$) in February in the location where the peak AOD occurs. Consequently, it is quite plausible for the ADRE maximum to occur in a different location than the AOD minimum. In Section 3.3, we provide a more in-depth analysis of the ADRE dependence on surface albedo and its role in explaining the contrast between water and land ADREs over northeastern China.

The main meteorological variables contributing to ADRE in February 2020 are T2M, QV2M, and f_L. Anomalies in T2M and QV2M are strongly positive over northeastern China and exceed 1.5 times the standard deviation of February anomalies for 2003–2020 (Figures 10a and 10b). Normalized anomalies in f_L are also positive north of the Yellow Sea (Figure 10c) but are smaller in magnitude. The corresponding contributions to ADRE are generally positive for T2M over the Yellow Sea region, strongly negative for QV2M, and weakly negative for f_L (Figures 10d–10f). Since QV2M normalized anomalies dominate over the other contributions, the sum of all contributions to ADRE is generally negative over northeastern China (Figure 7b). Contributions from other meteorological variables are much smaller compared to T2M and QV2M (not

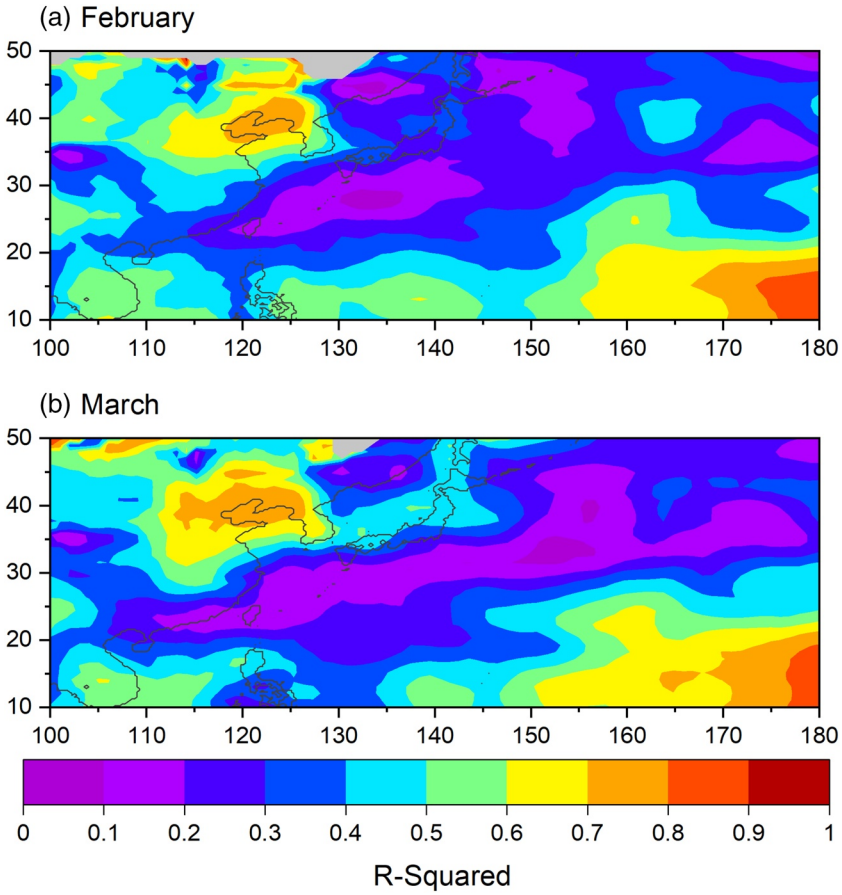

Figure 6. *R*-Squared values for multilinear regression fits to ADRE monthly anomalies using all (a) February and (b) March months between 2003 and 2020. ADRE, aerosol direct radiative effects.

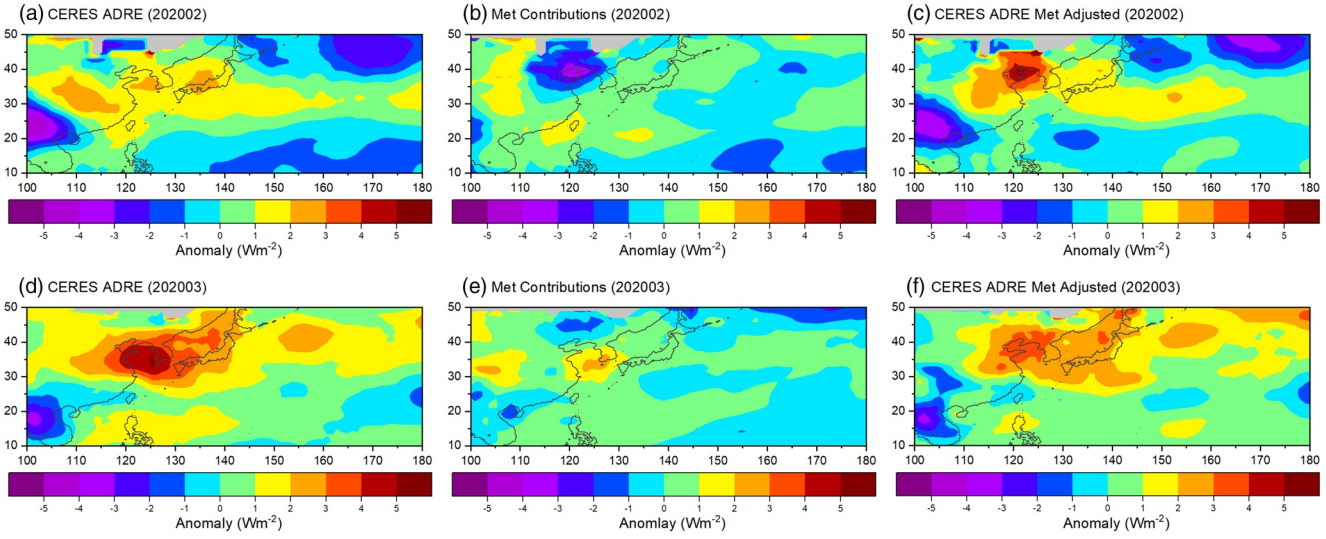

Figure 7. Anomalies of (a and d) CERES ADRE (b and e) sum of all terms in MLR analysis, and (e and f) ADRE after subtracting meteorological contributions for February 2020 (top) and March 2020 (bottom). CERES, Clouds and the Earth's Radiant Energy System; ADRE, aerosol direct radiative effects.

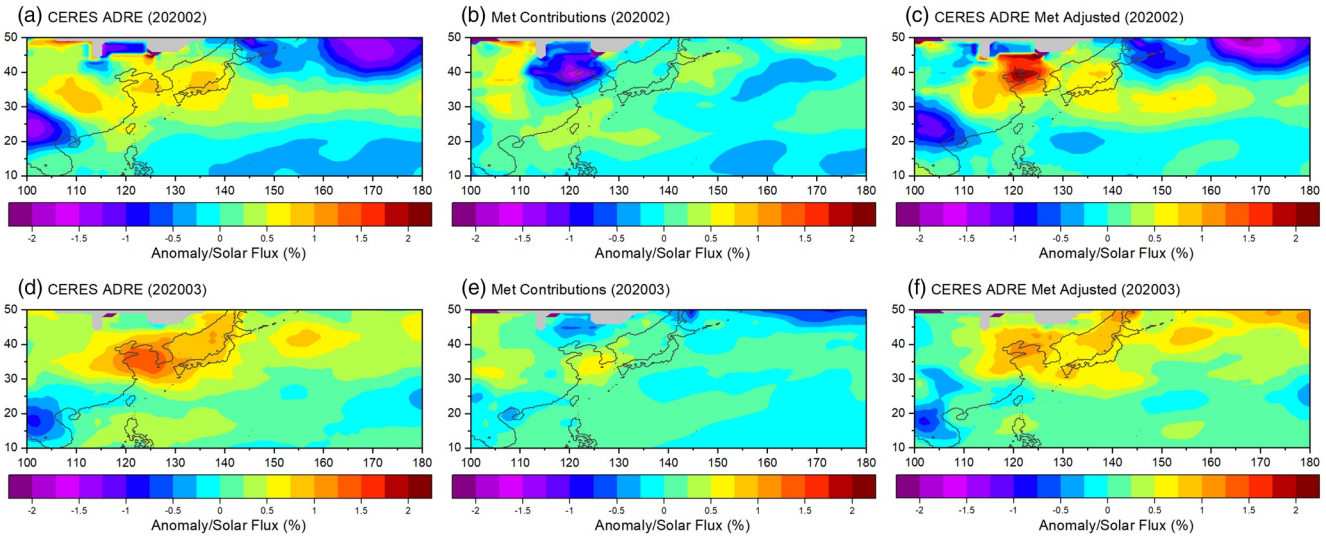

Figure 8. Same as Figure 7 except anomalies are normalized by solar flux.

shown). These results confirm earlier studies that noted hot, humid and hazy conditions in February 2020 (Chang et al., 2020; Diamond & Wood, 2020). Under such conditions, aerosol optical depth tends to be greater as aerosol size increases with increasing humidity, attenuating a greater fraction of the incident SW radiation. This in effect masked the true influence of the COVID-19 shutdown over China. During March meteorological conditions are also anomalously hot and humid, but now the normalized anomalies in T2M exceed those in QV2M over much of northeastern China (Figures 11a and 11b), implying drier conditions compared to February. Consistent with this finding, normalized anomalies in f_L are generally negative (Figure 11c). Because of the drier conditions, contributions to ADRE are generally positive overall (Figures 7e and 11d–11f).

To further highlight the impact of meteorology on ADRE during the COVID-19 shutdown, we focus our analysis on 30°–45°N and 115°–130°E, which includes regions that typically have high anthropogenic emissions of SO_2 (including biofuels), as well as a portion of the East Asian Marginal Seas (Figure 12a). We consider both land and ocean but exclude regions with snow. The climatological average ADRE in this region

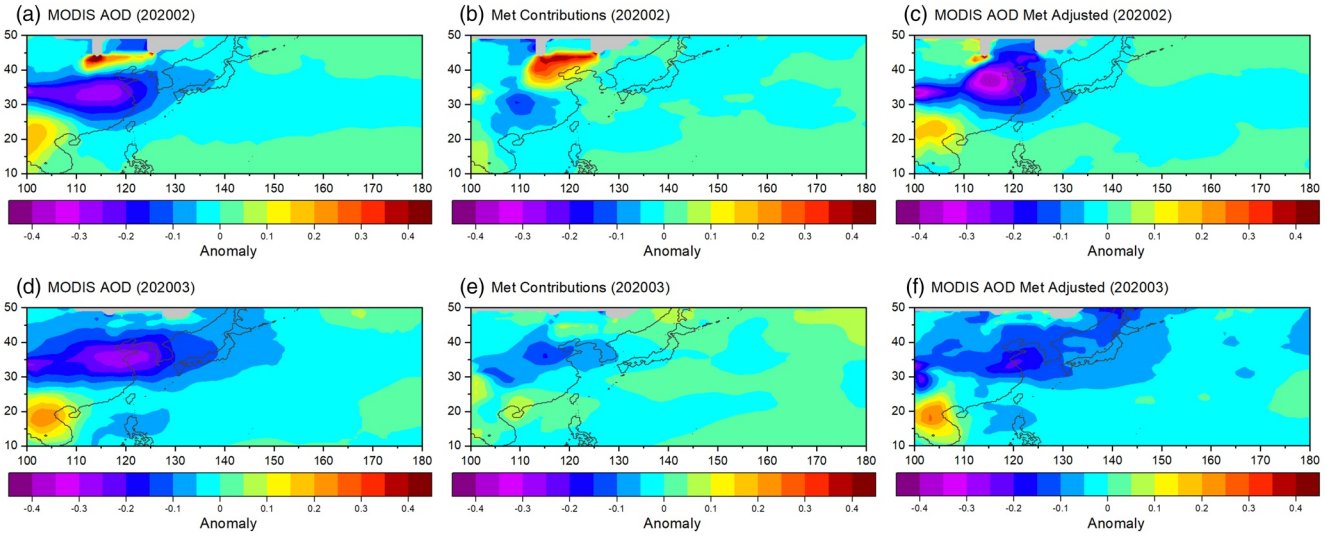

Figure 9. Anomalies of (a and d) MODIS AOD (b and e) sum of all terms in MLR analysis, and (e and f) AOD after subtracting meteorological contributions for February 2020 (top) and March 2020 (bottom). AOD, aerosol optical depth; MODIS, Moderate Resolution Spectroradiometer.

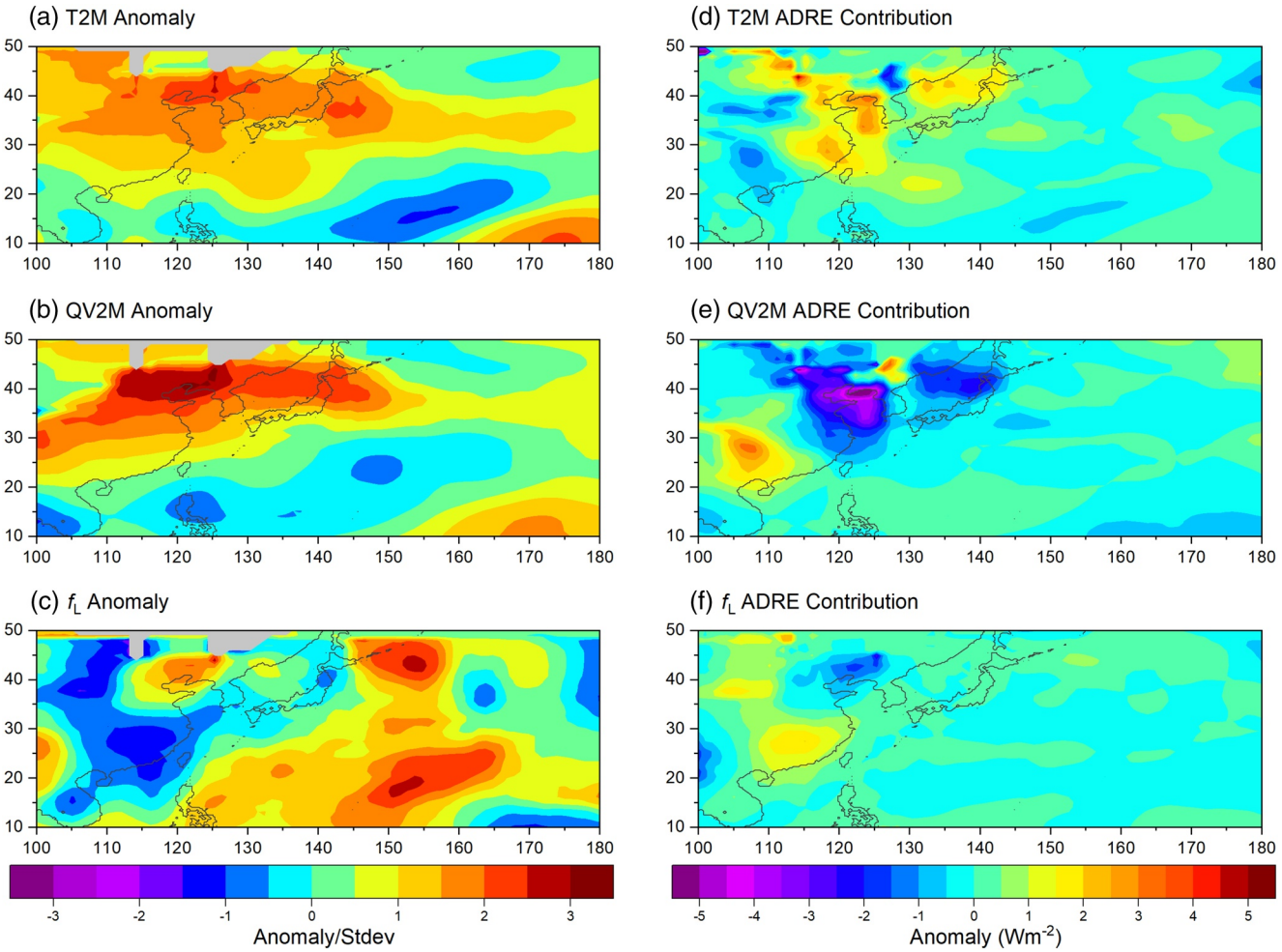

Figure 10. February 2020 anomalies of (a) 2-m air temperature (T2M), (b) 2-m specific humidity (QV2M), and (c) low cloud fraction (f_L) after normalizing by standard deviation. Multilinear regression ADRE contributions from (d) T2M, (e) QV2M, and (f) f_L. ADRE, aerosol direct radiative effects.

ranges from −7 Wm^{-2} during winter to −24 Wm^{-2} during summer (Figure 12b). In contrast, the climatological mean AOD is above the annual average between January and July, peaking at 0.67 in June, and remains below the annual average during the rest of the year (Figure 12c). The climatological mean AOD in March is only slightly (~5%) larger than the February mean value.

Monthly ADRE anomalies for 07/2002–03/2020 over the analysis domain shown in Figure 12a are provided in Figure 13a. There is a positive trend of 1.02 ± 0.53 Wm^{-2} per decade, corresponding to an increase in ADRE of 1.8 Wm^{-2} over 17.7 years. This is equivalent to a 13% increase relative to the climatological average and is primarily a result of reduced emissions. We note that March 2020 exceeds the 95% confidence interval (shown by cyan shading), but February 2020 remains well within the 95% confidence interval. To examine the sensitivity to the baseline climatology used, we repeated the analysis using a climatology for 2014–2019—well after pollution controls in China were in place—and arrived at the same conclusion (not shown).

When meteorological contributions to ADRE determined from the multilinear regression analysis are subtracted from the original ADRE anomalies, normalized by incoming solar flux and scaled by the climatological mean solar flux for 07/2002–06/2019, the trend is reduced to 0.65 ± 0.31 Wm^{-2} per decade (Figure 13b). In this case, the variability in ADRE is also reduced by 42%, and now both February and March 2020 exceed their respective climatological values by 23% and 22%, respectively, which is significant at the 95% confidence level. Since the increases in ADRE in February and March 2020 are partially due to long-term declines

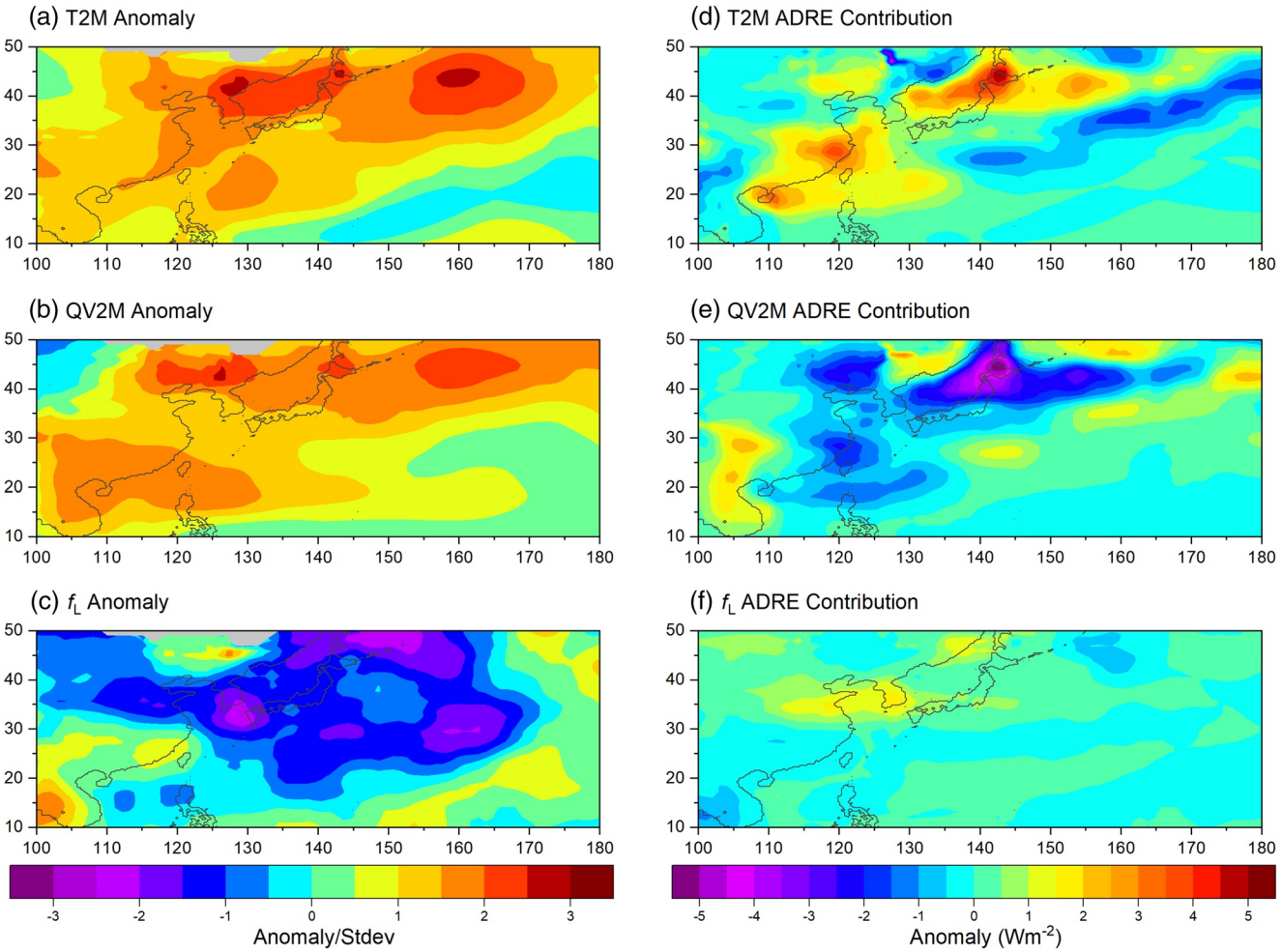

Figure 11. Same as Figure 10 but for March 2000.

in AOD that are independent of the COVID-19 shutdown, we also remove the long-term trend in ADRE by applying a linear least squares fit to the time series in Figure 13b and then subtract the fitted values from anomalies in Figure 13b. Even after removing the long-term trend, February and March 2020 still lie above the 95% confidence interval. In fact, February and March 2020 are the two largest positive ADRE anomalies in the time series and the only occurrence in which two consecutive months exceed the 95% confidence interval. Only two other months (02/2008 and 01/2007) show ADRE anomalies with greater magnitudes: in both cases, the ADRE anomalies are negative and occur well before pollution controls were put in place.

3.3. Water-Land Contrast in ADRE Anomalies and Trends

It is noteworthy that ADRE trends in Figure 1a and anomalies in Figures 5a and 5c over northeastern China are more pronounced over water than land, while the opposite is true for AOD (Figures 1b, 5b, and 5d). In contrast, trends in both ADRE and AOD over India and the United States show a smooth transition between water and land (Figures 1a and 1b). The reason is due to a strong water-land contrast in ADRE efficiency over northeastern China that is likely enhanced by strong absorption by aerosols. According to the emissions inventory used in Paulot et al. (2018), the 10-year average (2001–2010) rate of anthropogenic emission of black carbon (BC) over northeastern China exceeds that over both India and the United States during the CERES period (Figure 14). This is especially true for the land region west of the Yellow Sea. Compared to India, anthropogenic BC emissions rates in this region can be as much as six times higher.

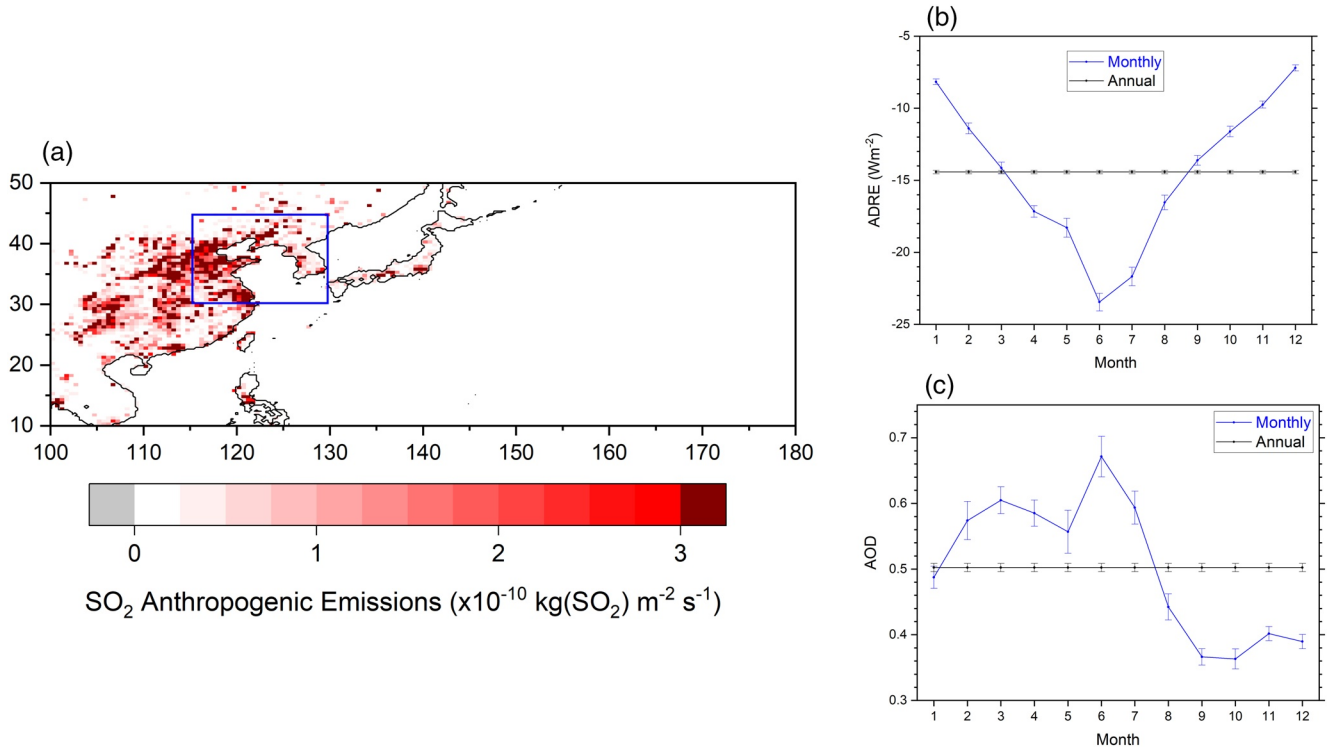

Figure 12. (a) Anthropogenic emissions of SO2 (including biofuels) for March 2005 from MEIC data set. (b and c) Climatological monthly and annual average (b) ADRE and (c) values for the domain corresponding to the box shown in (a), defined by 30°N–45°N; 115°E–130°E. ADRE, aerosol direct radiative effects.

The ADRE efficiencies over the water and land portions of the domain in northeastern China considered in Section 3.2 are shown in Figures 15a and 15b. To determine the ADRE efficiencies, we first divide the ADRE monthly anomalies by their corresponding monthly mean solar flux values and then multiply each by the water–land average solar flux ($<S_o>$) for 07/2002–06/2019. Over water, which primarily corresponds to the Yellow Sea region, the ADRE efficiency is -21 ± 1 Wm^{-2} τ^{-1}. For land, the ADRE is -8.9 ± 0.6 Wm^{-2} τ^{-1}. In both cases, there is a good correlation between CERES ADRE and MODIS AOD. Because of this large contrast in ADRE efficiency, the ADRE change over water can be twice that over land even for a smaller AOD change.

The reason why the ADRE efficiencies differ so much for water and land relates to differences in surface albedo and aerosol absorption. To illustrate, Figure 16 shows calculations of ADRE efficiency against surface albedo for a range of aerosol single scattering albedos (SSAs). The calculations are from the Langley Fu-Liou radiative transfer model (Fu & Liou, 1993; Fu et al., 1998; Kato et al., 1999, 2005; Kratz & Rose, 1999) using a combination of the Urban aerosol model of d'Almedia et al. (1991) and soot from the Optical Properties of Aerosols and Clouds (OPAC) database (Hess et al., 1998). The Urban AOD is held fixed at 0.5 and soot AOD is varied from 0.01 to 0.1, yielding total aerosol SSAs ranging from 0.82 to 0.94. Surface albedo is spectrally resolved over 18 wavelength bands corresponding to the Urban IGBP model used in determining CERES SYN1deg computed fluxes (Rutan et al., 2009). Variable surface albedos are obtained by simply scaling the spectral albedos. The ADRE efficiency is determined by differencing pristine and clear-sky SW TOA fluxes over a 24-h period on March 21 at latitude 39.9°N, which corresponds to Beijing, China.

In all cases, ADRE efficiency becomes less negative with increasing surface albedo. However, as aerosol absorption increases, sensitivity to surface albedo increases, meaning that in strongly absorbing conditions, even a small change in surface albedo can cause a large change in ADRE efficiency. For the domain in northeastern China shown in Figure 12a, the mean surface albedo over the water portion is 0.06 compared to 0.17 for land. The difference in ADRE efficiency for this change in surface albedo (12 Wm^{-2} τ^{-1}) is within the range of the theoretical values shown in Figure 16 for the same surface albedo change. We note that the absolute values of computed ADRE efficiencies in Figure 16 are not directly comparable to those derived

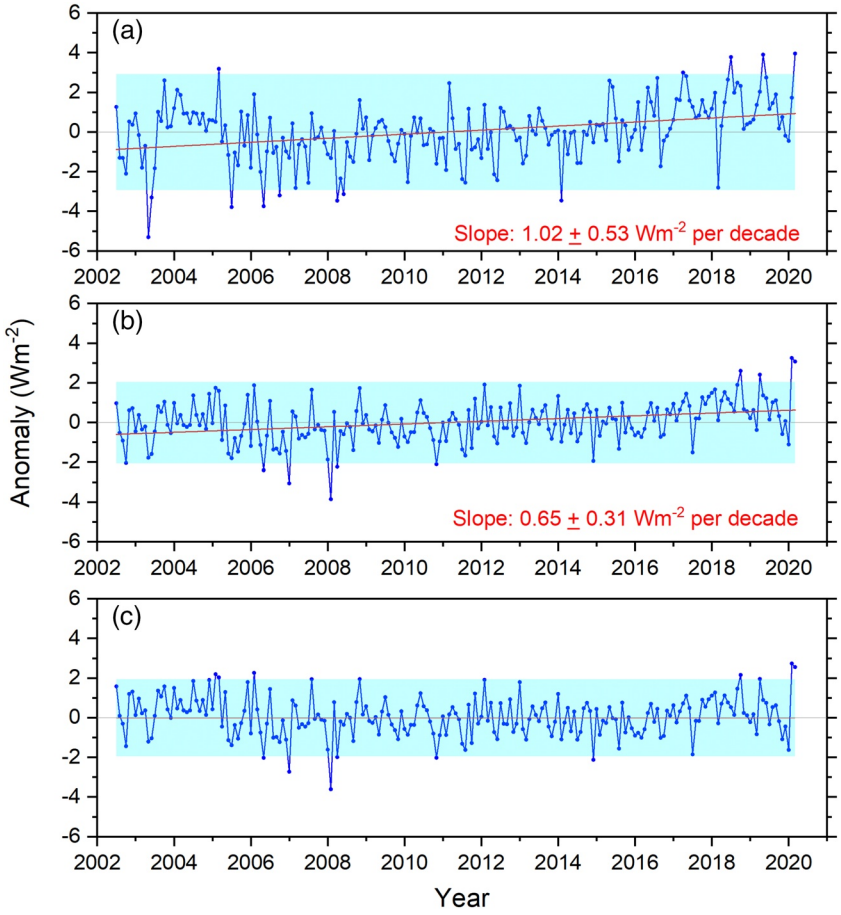

Figure 13. Monthly anomalies in ADRE for 30°N–45°N and 115°E–130°E (excluding snow) after: (a) no adjustments, (b) adjusting for meteorology and incoming solar flux, (c) adjusting for meteorology, incoming solar flux and the long-term trend. Cyan region corresponds to 95% confidence interval. ADRE, aerosol direct radiative effects.

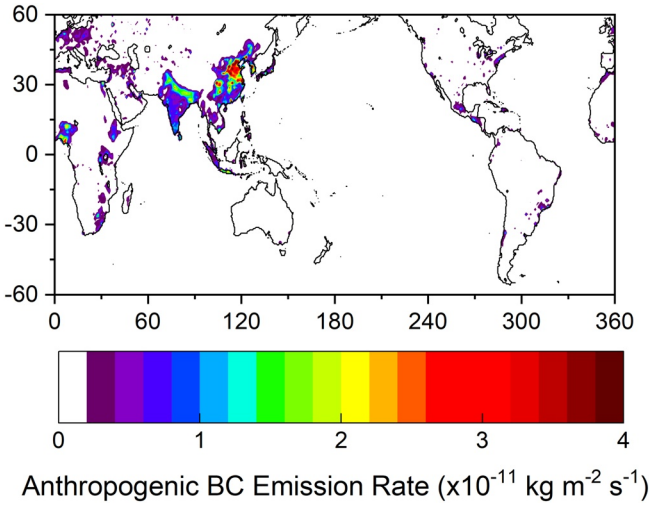

Figure 14. Anthropogenic black carbon (BC) emission rate averaged over 2001–2010. Anthropogenic emission sources include agriculture, energy, industrial, transportation, residential, commercial and other, solvents production and application, and waste (Zhang et al., 2009).

from the observations since the calculations are determined for an idealized case on one day (March 21) in one location.

Another contributing factor to the water-land contrast in ADRE efficiency could be due to differences between the aerosol properties over the water and land. If the land aerosols are more absorbing than those that are transported over the water, this could further enhance the water-land contrast in ADRE efficiency beyond that caused by water-land differences in surface albedo.

The situation over India is quite different. Figures 17a and 17b show the trends in the atmospheric and surface contributions to ADRE. The atmospheric contribution is the first term on the right-hand-side of Equation 4 and the surface contribution is the difference term in square brackets (aerosol masking term). Over India, there is a negative trend for the surface contribution to ADRE (Figure 17b), which adds to the negative trend in the atmospheric contribution (Figure 17a). The negative ADRE trend in the surface contribution occurs because of a decreasing trend in surface albedo, which further increases ADRE sensitivity to AOD. Chrysoulakis et al. (2019) also find a negative trend in surface albedo over India for 2000–2015 using the MODIS MCD43A1 and MCD43A2 data products (Lucht et al., 2000; Schaaf et al., 2002), which are not used in CERES

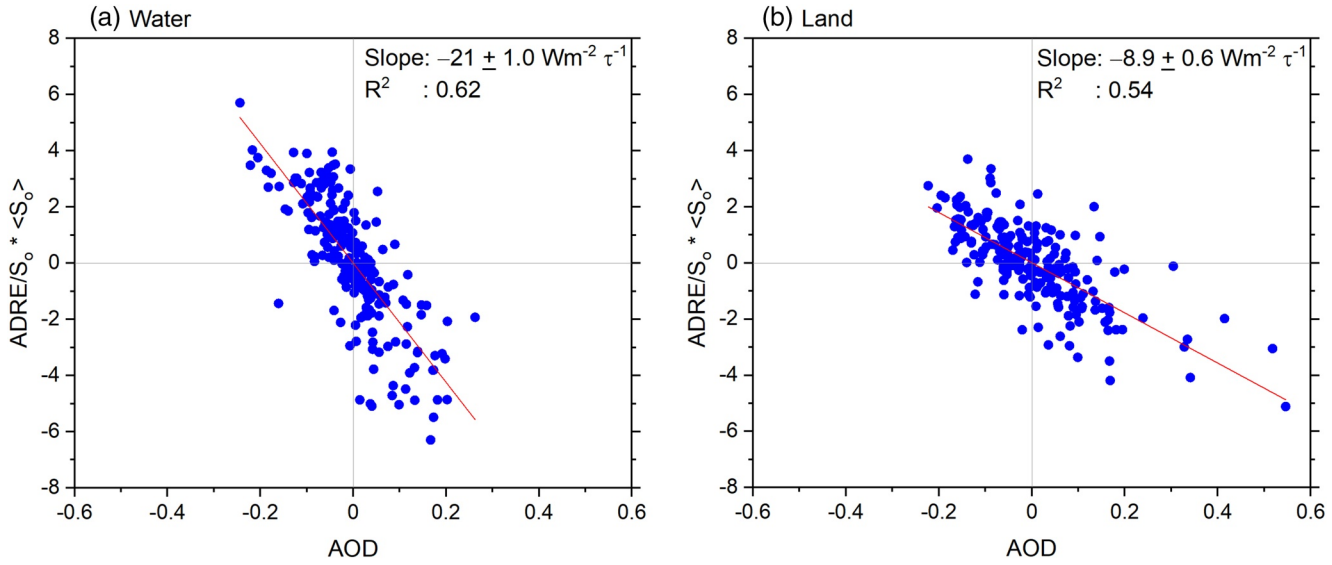

Figure 15. ADRE against AOD for the (a) water and (b) land portion of the domain in northeastern China shown in Figure 12a. ADRE, aerosol direct radiative effects; AOD, aerosol optical depth.

processing. The reason for the decrease in surface albedo is due to an increase in summer monsoon rainfall over India since 2002, following a decline during the second half of the 20th century (Jin & Wang, 2017).

4. Summary

Observations from CERES and MODIS are used to examine trends and variations in clear-sky shortwave ADRE and AOD between July 2002 and March 2020. The ADRE is determined with a new approach that uses a SW decomposition technique that enables attribution of ADRE changes in terms of atmospheric (primarily AOD) and surface albedo changes.

Positive trends in ADRE (less reflection to space) and negative trends in AOD are observed over China, the United States, South America, and Europe, whereas ADRE decreases (more reflection to space) and AOD increases occur over India. Similar results have been found from regional clear-sky surface irradiance measurements over China (S. Yang et al., 2019), Europe (Garcia et al., 2013; Manara et al., 2016), and the United States (Gan et al., 2014). At the global scale, trends in both ADRE and AOD fall within their respective 95% confidence intervals. However, ADRE shows a significant increase over the NH while the AOD trend is near zero there. In contrast, there is an unexpected positive trend in AOD over the SH that is not present in ADRE. The positive AOD trend is widespread and primarily occurs over ocean. The reason for this discrepancy is unclear—a calibration drift in MODIS cannot be discounted as a possible cause. Nevertheless, we find excellent agreement in monthly anomalies between ADRE and AOD, with an *R*-square of 0.81 over the NH and 0.71 globally. At global and hemispheric scales, we do not see a noticeable impact from the global economic shutdown associated with COVID-19. The largest anomalies at these scales are associated with major fire events, such as the Siberian fires in May 2003, Indonesian fires during fall 2015, and the Australian bushfires during late 2019 and early 2020.

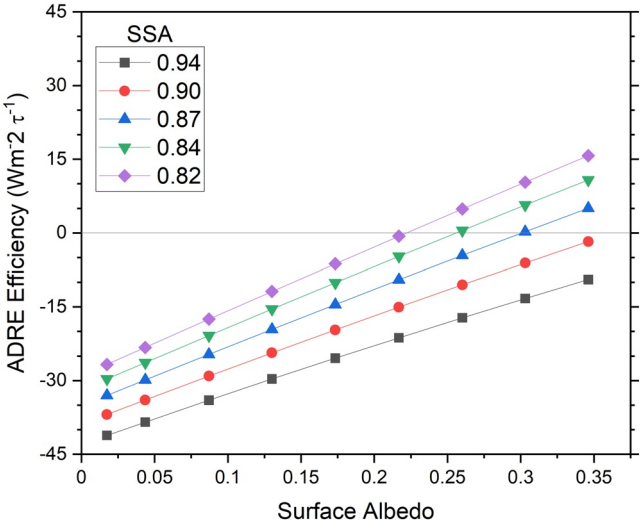

Figure 16. Theoretical ADRE efficiency against surface albedo for different aerosol SSA. ADRE, aerosol direct radiative effects; SSA, single scattering albedo.

During early 2020, the COVID-19 shutdown had a noticeable impact on ADRE and AOD over China and the East Asian Marginal Seas. However, anomalies in both ADRE and AOD were far more pronounced in March than February even though the shutdown had its greatest impact on the

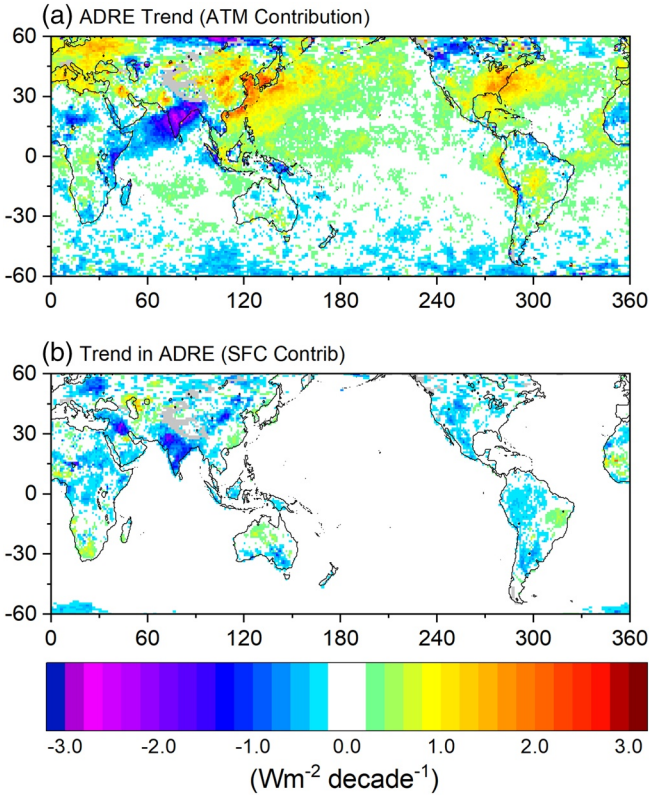

Figure 17. Trends in the (a) atmospheric and (b) surface contributions to ADRE anomalies for 2002/07–2020/03. ADRE, aerosol direct radiative effects.

Chinese economy and manufacturing in February. The reason for this unexpected finding is due to the influence of meteorology. During February, conditions were hot and humid, with anomalies in specific humidity greater than two times the standard deviation of all February anomalies over the record. To account for the influence of meteorology, we apply a multilinear regression analysis to remove the influence of meteorology from ADRE and AOD anomalies. After accounting for meteorology and normalizing by incident solar flux, ADRE anomalies in February exceed those in March over northeastern China, consistent with expectation. A similar analysis applied to AOD leads to the same conclusion. Focusing on a region that includes the Yellow Sea and surrounding land area (30°–45°N and 115°–130°E), we find that when meteorology is accounted for, variability in ADRE is reduced by 42% and both February and March 2020 exceed their respective climatological values by 23% and 22%, respectively. Furthermore, February and March 2020 now correspond to the two largest positive ADRE anomalies in the time series and the only occurrence in which two consecutive months exceed the 95% confidence interval. This is true even after removing the long-term trend in ADRE. We thus conclude that the influence of the COVID-19 shutdown on ADRE and AOD was significant but was largely masked by anomalous meteorological conditions.

Comparisons between regional patterns in ADRE and AOD anomalies and trends over northeastern China show some apparent water-land inconsistencies that are unique to this region. While trends in AOD exhibit smooth transitions at water-land boundaries, ADRE trends are strongly positive over water—particularly over the Yellow Sea—and much weaker over land. Similarly, the greatest reduction in AOD during the COVID-19 economic shutdown occurs over land to the southwest of the maximum in ADRE, which lies over the Yellow Sea.

The reason for these apparent discrepancies is because ADRE depends not only upon AOD but also surface albedo. When surface albedo is low, the SW radiative cooling effect of aerosol for a given AOD increase is greater than for a surface with a higher albedo. The sensitivity to surface albedo is even more pronounced when the concentration of absorbing aerosols is high, such as over northeastern China. As a result, it is quite plausible to see a stronger radiative cooling effect of aerosols over water than land, even if the AOD change is greater over land. The situation over India differs markedly from that over northeastern China as there is a positive trend in AOD and a negative trend in land surface albedo. Both contribute to a negative ADRE trend over land, which reduces any water-land contrast.

Data Availability Statement

The CERES EBAF Ed4.1, SYN1deg Edition4A, and CERES SSF1deg Edition4A data sets were downloaded from https://ceres.larc.nasa.gov/data/. The Niño 3.4 index data are from http://www.esrl.noaa.gov/psd/data/correlation/nina34.data. MERRA-2 and MODIS MYD08_M3.061 550 nm AOD Dark Target + Deep Blue Combined data were obtained from the Giovanni online data system, developed, and maintained by the NASA GES DISC.

Acknowledgments
This research has been supported by NASA CERES project. We would like to thank Dr. Seiji Kato and Mr. Fred Rose for their helpful comments.

References

Ackerman, S. A., Platnick, S., Bhartia, P. K., Duncan, B., L'Ecuyer, T., Heidinger, A., et al. (2019). Satellites see the world's atmosphere. *Meteorological Monographs*, *59*(4), 4.1–4.53. https://doi.org/10.1175/AMSMONOGRAPHS-D-18-0009.1

Bellouin, N. J., Davies, W., Shine, K. P., Quaas, J., Mulmenstadt, J., et al. (2020). Radiative forcing of climate change from the Copernicus reanalysis of atmospheric composition. *Earth System Science Data*, *12*, 1649–1677. https://doi.org/10.5194/essd-12-1649-2020

Bellouin, N. J., Quaas, J., Gryspeerdt, E., Kinne, S., Stier, P., Watson-Parris, D., et al. (2020). Bounding global aerosol radiative forcing of climate change. *Reviews of Geophysics*, *58*, e2019RG000660. https://doi.org/10.1029/2019RG000660

Bhatt, R., Doelling, D. R., Scarino, B. R., Gopalan, A., Haney, C. O., Minnis, P., & Bedka, K. M. (2016). A consistent AVHRR visible calibration record based on multiple methods applicable for the NOAA degrading orbits. Part I: Methodology. *Journal of Atmospheric and Oceanic Technology*, *33*, 2499–2515. https://doi.org/10.1175/JTECH-D-16-0044

Brest, C. L., & Rossow, W. B. (1992). Radiometric calibration and monitoring of NOAA AVHRR data for ISCCP. *International Journal of Remote Sensing*, *13*, 235–273. https://doi.org/10.1080/01431169208904037

Brodzik, M. J., & Stewart, J. S. (2016). *Near-Real-Time SSM/I-SSMIS EASE-Grid Daily Global Ice Concentration and Snow Extent, version 5*: NASA National Snow and Ice Data Center Distributed Active Archive Center. https://doi.org/10.5067/3KB2JPLFPK3R

Ceppi, P., & Hartmann, D. L. (2015). Connections between clouds, radiation, and midlatitude dynamics: A review. *Current Climate Change Reports*, *1*, 94–102.

Chang, Y., Huang, R.J., Ge, X., Huang, X., Hu, J., Duan, Y., et al. (2020). Puzzling haze events in China during the coronavirus (COVID-19) shutdown. *Geophysical Research Letters*, *47*, e2020GL088533. https://doi.org/10.1029/2020GL088533

Chrysoulakis, N., Mitraka, Z., & Gorelick, N. (2019). Exploiting satellite observations for global surface albedo trends monitoring. *Theoretical and Applied Climatology*, *137*, 1171–1179. https://doi.org/10.1007/s00704-018-2663-6

Collins, W. D., Rasch, P. J., Eaton, B. E., Khattatov, B. V., Lamarque, J.-F., & Zender, C. S. (2001). Simulating aerosols using a chemical transport model with assimilation of satellite aerosol retrievals: Methodology for INDOEX. *Journal of Geophysical Research*, *106*(D7), 7313–7336.

Damoah, R., Spichtinger, N., Forster, C., James, P., Mattis, I., Wandinger, U., et al. (2004). Around the world in 17 days – hemispheric-scale transport of forest fire smoke from Russia in May 2003. *Atmospheric Chemistry and Physics*, *4*, 1311–1321.

Derimian, Y., Dubovik, O., Huang, X., Lapyonok, T., Litvinov, P., Kostinski, A. B., et al. (2016). Comprehensive tool for calculation of radiative fluxes: Illustration of shortwave aerosol radiative effect sensitivities to the details in aerosol and underlying surface characteristics. *Atmospheric Chemistry and Physics*, *16*, 5763–5780. https://doi.org/10.5194/acp-16-5763-2016

Diamond, M. S., & Wood, R. (2020). Limited regional aerosol and cloud microphysical changes despite unprecedented decline in nitrogen oxide pollution during the February 2020 COVID-19 shutdown in China. *Geophysical Research Letters*, *47*, e2020GL088913. https://doi.org/10.1029/2020GL088913

D'Almeida, G. A., Koepke, P., & Shettle, E. P. (1991). *Atmospheric climatologyand radiative characteristics*. Hampton, VA: A. Deepak.

Evan, A. T., Foltz, G. R., Zhang, D., & Vimont, D. J. (2011). Influence of African dust on ocean–atmosphere variability in the tropical Atlantic. *Nature Geoscience*, *4*, 762–765. https://doi.org/10.1038/NGEO1276

Feng, J., Zhu, J., Li, J., & Liao, H. (2020). Aerosol concentrations variability over China: Two distinct leading modes. *Atmospheric Chemistry and Physics*, *20*, 9883–9893. https://doi.org/10.5194/acp-20-9883-2020

Field, R. D., Hickman, J. E., Geogdzhayev, I. V., Tsigaridis, K., & Bauer, S. E. (2020). Changes in satellite retrievals of atmospheric composition over eastern China during the 2020 COVID-19 lockdowns. *Atmospheric Chemistry and Physics*. https://doi.org/10.5194/acp-2020-567

Frey, R. A., Ackerman, S. A., Liu, Y., Strabala, K. I., Zhang, H., Key, J. R., & Wang, X. (2008). Cloud Detection with MODIS. Part I: Improvements in the MODIS Cloud Mask for Collection 5. *Journal of Atmospheric and Oceanic Technology*, *25*, 1057–1072. https://doi.org/10.1175/2008JTECHA1052.1

Fu, Q., Lesins, G., Higgins, J., Charlock, T., Chylek, P., & Michalsky, J. (1998). Broadband water vapor absorption of solar radiation tested using ARM data. *Geophysical Research Letters*, *25*, 1169–1172. https://doi.org/10.1029/98GL00846

Fu, Q., & Liou, K.-N. (1993). Parameterization of the radiative properties of cirrus clouds. *Journal of the Atmospheric Sciences*, *50*, 2008–2025. https://doi.org/10.1175/1520-0469(1993)050,2008:POTRPO.2.0.CO;2

Gan, C. M., Pleim, J., Mathur, R., Hogrefe, C., Long, C. N., Xing, J., et al., 2014: Assessment of the effect of air pollution controls on trends in shortwave radiation over the United States from 1995 through 2010 from multiple observation networks. *Atmospheric Chemistry and Physics 14*, 1701–1715. https://doi.org/10.5194/1Acp-14-1701-2014

Garcia, R. D., Cuevas, E., Garcia, O. E., Cachorro, V. E., Palle, P., Bustos, J. J., et al. (2013). Reconstruction of global solar radiation time series from 1933 to 2013 at the Izana Atmospheric Observatory. *Atmospheric Measurement Techniques*, *2014*(7), 3139–3150

Gelaro, R., McCarty, W., Suárez, M. J., Todling, R., Molod, A., Takacs, L., et al. (2017). The modern-era retrospective analysis for research and applications, Version 2 (MERRA-2). *Journal of Climate*, *30*, 5419–5454. https://doi.org/10.1175/JCLI-D-16-0758.1

Hammer, M. S., van Donkelaar, A., Li, C., Lyapustin, A., Sayer, A.M., Hsu, N. C., et al. (2020). Global estimates and long-term trends of fine particulate matter concentrations (1998–2018). *Environmental Science & Technology*, *54*(13), 7879–7890. https://doi.org/10.1021/acs.est.0c01764

Harris, E. S. (1991). Tracking the economy with the purchasing managers' index. *Federal Reserve Bank of New York Quarterly Review, Autumn*, *16*, 61–69.

Heidinger, A. K., Straka, W. C., III, Molling, C. C., & Sullivan, J. T. (2010). Deriving an inter-sensor consistent calibration for the AVHRR solar reflectance data record. *International Journal of Remote Sensing*, *31*, 6493–6517. https://doi.org/10.1080/01431161.2010.496472

Hess, M., Koepke, P., & Schult, I. (1998). Optical properties of aerosols and clouds: The software package OPAC. *Bulletin of the American Meteorological Society*, *79*, 831–844.

Hsu, N. C., Lee, J., Sayer, A. M., Kim, W., Bettenhausen, C., Tsay, S.-C., 2019: VIIRS deep blue aerosol products over land: Extending the EOS long-term aerosol data records. *Journal of Geophysical Research - D: Atmospheres*, *124* (7), 4026–4053.

Huang, X., Ding, A., Gao, J., Zheng, B., Zhou, D., Qi, X., et al. (2020). Enhanced secondary pollution offset reduction of primary emissions during COVID-19 lockdown in China. *National Science Review*, *8*, nwaa137. https://doi.org/10.1093/nsr/nwaa137

Imhoff, M. L., Wolfe, R., Diner, D. J., Chopping, M., Kahn, R., Salomonson, V., et al. (2009). An overview of terra mission results related to the carbon cycle. *Geography Compass*, *3*. https://doi.org/10.1111/j.1749-8198.2008.00183.x

Jin, Q., & Wang, C. (2017). A revival of Indian summer monsoon rainfall since 2002. *Nature Climate Change*, *7*, 587–595. https://doi.org/10.1038/NCLIMATE3348

Karlsson, K. G., Riihela, A., Muller, R., Meirink, J. F., Sedlar, J., Stengel, M., et al. (2013). CLARA-A1: A cloud, albedo, and radiation dataset from 28 yr of global AVHRR data. *Atmospheric Chemistry and Physics*, *13*, 5351–5367.

Kato, S., Ackerman, T., Mather, J., & Clothiaux, E. (1999). The k-distribution method and correlated-k approximation for a shortwave radiative transfermodel. *Journal of Quantitative Spectroscopy & Radiative Transfer*, *62*, 109–121. https://doi.org/10.1016/S0022-4073(98)00075-2

Kato, S., Rose, F. G., & Charlock, T. P. (2005). Computation of domain-averaged irradiance using satellite-derived cloud properties. *Journal of Atmospheric and Oceanic Technology*, *22*, 146–164. https://doi.org/10.1175/JTECH-1694.1

Kato, S., Rose, F. G., Rutan, D. A., Thorsen, T. E., Loeb, N. G., Doelling, D. R., et al. (2018). Surface irradiances of edition 4.0 Clouds and the Earth's Radiant Energy System (CERES) Energy Balanced and Filled (EBAF) data product. *Journal of Climate*, *31*, 4501–4527. https://doi.org/10.1175/JCLI-D-17-0523.1

Kato, S., Rutan, D. A., Rose, F. G., Caldwell, T. E., Ham, S., Radkevich, A., et al. (2020). Uncertainty in satellite-derived surface irradiances and challenges in producing surface radiation budget climate data record. *Remote Sensing*, *12*(12), 1950. https://doi.org/10.3390/rs12121950

Koplitz, S. N., Mickley, L. J., Marlier, M. E., Buonocore, J. J., Kim, P. S., Liu, T., et al. (2016). Public health impacts of the severe haze in Equatorial Asia in September–October 2015: Demonstration of a new framework for informing fire management strategies to reduce downwind smoke exposure. *Environmental Research Letters*, *11*, 094023. https://doi.org/10.1088/1748-9326/11/9/094023

Kratz, D. P., & Rose, F. G. (1999). Accounting for molecular absorption within the spectral range of the CERES window channel. *Journal of Quantitative Spectroscopy & Radiative Transfer*, *61*, 83–95. https://doi.org/10.1016/S0022-4073(97)00203-3

Lee, K. H., Kim, J. E., Kim, Y. J., Kim, J., & Hoyningen-Huene, W. (2005). Impact of the smoke aerosol from Russian forest fires on the atmospheric environment over Korea during May 2003. *Atmospheric Environment*, *39*, 85–99. https://doi.org/10.1016/j.atmosenv.2004.09.032

Levy, R. C., Mattoo, S., Munchak, L. A., Remer, L. A., Sayer, A. M., Patadia, F., & Hsu, N. C. (2013). The Collection 6 MODIS aerosol products over land and ocean. *Atmospheric Measurement Techniques*, *6*, 2989–3034. https://doi.org/10.5194/amt-6-2989-2013

Le, T., Wang, Y., Liu, L., Yang, J., Yung, Y. L., Li, G., & Seinfeld, J. H. (2020). Unexpected air pollution with marked emission reductions during the COVID-19 outbreak in China. *Science*, *369*, eabb7431. https://doi.org/10.1126/science.abb7431

Loeb, N. G., Doelling, D. R., Wang, H., Su, W., Nguyen, C., Corbett, J. G., et al. (2018). Clouds and the Earth's Radiant Energy System (CERES) Energy Balanced and Filled (EBAF) Top-of-Atmosphere (TOA) edition 4.0 data product. *Journal of Climate*, *31*, 895–918. https://doi.org/10.1175/JCLI-D-17-0208.1

Loeb, N. G., Su, W., & Kato, S. (2016). Understanding climate feedbacks and sensitivity using observations of Earth's energy budget. *Current Climate Change Reports*, *2*(2016), 170–178. https://doi.org/10.1007/s40641-016-0047-5

Loeb, N. G., Thorsen, T. J., Norris, J. R., Wang, H., & Su, W. (2018). Changes in Earth's energy budget during and after the "Pause" in global warming: An observational perspective. *MDPI Climate*, *6*, 62. https://doi.org/10.3390/cli6030062

Loeb, N. G., Wang, H., Rose, F. G., Kato, S., Smith, W. L., Jr., & Sun-Mack, S. (2019). Decomposing shortwave top-of-atmosphere and surface radiative flux variations in terms of surface and atmospheric contributions. *Journal of Climate*, *32*, 5003–4019. https://doi.org/10.1175/JCLI-D-18-0826.1

Lucht, W., Schaaf, C. B., & Strahler, A. H. (2000). An algorithm for the retrieval of albedo from space using semiempirical BRDF models. *IEEE Transactions on Geoscience and Remote Sensing*, *38*, 977–998.

Mace, G. G., & Berry, E. (2017). Using active remote sensing to evaluate cloud-climate feedbacks: A review and a look to the future. *Current Climate Change Reports*, *3*, 185–192. https://doi.org/10.1007/s40641-017-0067-9

Manara, V., Brunetti, M., Celozzi, A., Maugeri, M., Sanchez-Lorenzo, A., & Wild, M. (2016). Detection of dimming/brightening in Italy from homogenized all-sky and clear-sky surface solar radiation records and underlying causes (1959-2013). *Atmospheric Chemistry and Physics*, *16*, 11145–11161. https://doi.org/10.5194/acp-16-11145-2016

Mishchenko, M. I., Geogdzhayev, I. V., Rossow, W. B., Cairns, B., Carlson, B. E., Lacis, A. A., et al. (2007). Long-term satellite record reveals likely recent aerosol trend. *Science*, *315*, 1543

Parkinson, C. L. (2013). Summarizing the first ten years of NASA's Aqua mission. *IEEE Journal of Selected Topics in Applied Earth Observations and Remote Sensing*, *6*(3), 1179–1188. https://doi.org/10.1109/JSTARS.2013.2239608

Paulot, F., Paynter, D., Ginoux, P., Naik, V., & Horowitz, L. W. (2018). Changes in the aerosol direct radiative forcing from 2001 to 2015: Observational constraints and regional mechanisms. *Atmospheric Chemistry and Physics*, *18*(2018), 13265. https://doi.org/10.5194/acp-18-13265-2018

Ramanathan, V., Crutzen, P. J., Kiehl, J. T., & Rosenfeld, D. (2001). Aerosols, climate, and the hydrological cycle. *Science*, *294*, 2119–2124. https://doi.org/10.1126/science.1064034

Remer, L. A., Levy, R.C., Mattoo, S., Tanré, D., Gupta, P., Shi, Y., et al. (2020). The dark target algorithm for observing the global aerosol system: Past, present and future. *Remote Sens*, *12*, 2900. https://doi.org/10.3390/rs12182900

Rutan, D. A., Kato, S., Doelling, D. R., Rose, F. G., Nguyen, L. T., & Caldwell, T. E. (2015). CERES synoptic product: Methodology and validation of surface radiant flux. *Journal of Atmospheric and Oceanic Technology*, *32*, 1121–1143. https://doi.org/10.1175/JTECH-D-14-00165.1

Rutan, D. A., Rose, F., Roman, M., Manalo-Smith, N., Schaaf, C., & Charlock, T. (2009). Development and assessment of broadband surface albedo from clouds and the Earth's radiant energy system clouds and radiation swath data product. *Journal of Geophysical Research*, *114*, D08125. https://doi.org/10.1029/2008JD010669

Santer, B. D., Wigley, T. M. L., Boyle, J. S., Gaffen, D. J., Hnilo, J. J., Nychka, D., et al. (2000). Statistical significance of trends and trend differences in layer-average atmospheric temperature time series. *Journal of Geophysical Research*, *105*, 7337–7356.

Sawyer, V., Levy, R. C., Mattoo, S., Cureton, G., Shi, Y., & Remer, L. A. (2020). Continuing the MODIS dark target aerosol time series with VIIRS. *Remote Sens*, *308*. https://doi.org/10.3390/rs12020308

Sayer, A. M., Munchak, L. A., Hsu, N. C., Levy, R. C., Bettenhausen, C., & Jeong, M. J. (2014). MODIS collection 6 aerosol products: Comparison between Aqua's e-Deep Blue, Dark Target, and "merged" data sets, and usage recommendations. *Journal of Geophysical Research - D: Atmospheres*, *119*, 13965–13989. https://doi.org/10.1002/2014jd022453

Schaaf, C. B., Gao, F., Strahler, A. H., Lucht, W., Li, X., Tsang, T., et al. (2002). First operational BRDF, albedo, nadir reflectance products from MODIS. *Remote Sensing of Environment*, *83*, 135–148

Stephens, G. L., O'Brien, D., Webster, P. J., Pilewski, P., Kato, S., & Li, J.-l. (2015). The albedo of Earth. *Reviews of Geophysics*, *53*, 141–163. https://doi.org/10.1002/2014RG000449

Su, W., Liang, L., Wang, H., & Eitzen, Z. A. (2020). Uncertainties in CERES top-of-atmosphere fluxes caused by changes in accompanying imager. *Remote Sensing*, *12*(12), 2040. https://doi.org/10.3390/rs12122040

Tao, M., Wang, L., Liangfu, C., Zifeng, W., & Tao, J. (2020). Reversal of aerosol properties in Eastern China with rapid decline of anthropogenic emissions. *Remote Sensing. MDPI*, *12*, 523. https://doi.org/10.3390/rs12030523

Trepte, Q. Z., Minnis, P., Sun-Mack, S., Yost, C. R., Chen, Y., Jin, Z., et al. (2019). Global cloud detection for CERES edition 4 using Terra and Aqua MODIS data. *IEEE Transactions on Geoscience and Remote Sensing*, *57*, 1–40. https://doi.org/10.1109/TGRS.2019.2926620

Wang, P., Chen, K., Zhu, S., Wang, P., & Zhang, H. (2020). Severe air pollution events not avoided by reduced anthropogenic activities during COVID-19 outbreak. *Resources, Conservation and Recycling*, *158*, 104814. https://doi.org/10.1016/j.resconrec.2020.104814

Wood, R., & Bretherton, C. S. (2006). On the relationship between stratiform low cloud cover and lower-tropospheric stability. *Journal of Climate*, *19*, 6425–6432. https://doi.org/10.1175/JCLI3988.1

Yang, Y., Liao, H., & Lou, S. (2016). Increase in winter haze over eastern China in recent decades: Roles of variations in meteorological parameters and anthropogenic emissions. *Journal of Geophysical Research - D: Atmospheres*, *121*(13), 065. https://doi.org/10.1002/2016JD025136050–13

Yang, S., Wang, X. L., & Wild, M. (2019). Causes of dimming and brightening in China inferred from homogenized daily clear-sky and all-sky in situ surface solar radiation records (1958-2016). *Journal of Climate*, *32*, 5901–5913. https://doi.org/10.1175/JCLI-D-18-0666.1.34

Yu, P., Xu, R., Abramson, M. J., Li, S., & Guo, Y. (2020). Bushfires in Australia: A serious health emergency under climate change. *Lancet Planet. Health*, *4*, 7–8. https://doi.org/10.1016/S2542-5196(19)30267-0

Yuan, T., Oreopoulos, L., Platnick, S. E., & Meyer, K. (2018). Observations of local positive low cloud feedback patterns and their role in internal variability and climate sensitivity. *Geophysical Research Letters*, *45*, 4438–4445. https://doi.org/10.1029/2018GL077904

Zhang, Q., Streets, D. G., Carmichael, G. R., He, K. B., Huo, H., Kannari, A., et al. (2009). Asian emissions in 2006 for the NASA INTEX-B mission. *Atmospheric Chemistry and Physics*, *9*, 5131–5153.

Zhao, B., Jiang, J. H., Gu, Y., Diner, D., Worden, J., Liou, K.-N., et al. (2017). Decadal-scale trends in regional aerosol particle properties and their linkage to emission changes. *Environmental Research Letters*, *2017*(12), 054021.